Received: 3 April 2019 | Revised: 30 May 2019 | Accepted: 12 June 2019

DOI: 10.1002/ese3.458

Energy Science & Engineering Open Access

RESEARCH ARTICLE

A comparative study of the nanopore structure characteristics of coals and Longmaxi shales in China

Shangwen Zhou[1,2] | **Honglin Liu**[1,2] | **Hao Chen**[1,2] | **Hongyan Wang**[1,2] | **Wei Guo**[1,2] | **Dexun Liu**[1,2] | **Qin Zhang**[1,2] | **Jin Wu**[1,2] | **Weijun Shen**[3]

[1]PetroChina Research Institute of Petroleum Exploration & Development, Beijing, China

[2]National Energy Shale Gas R&D (Experiment) Center, Langfang, China

[3]Institute of Mechanics, Chinese Academy of Sciences, Beijing, China

Correspondence
Honglin Liu, PetroChina Research Institute of Petroleum Exploration & Development, Beijing 100083, China.
Email: liuhonglin69@petrochina.com.cn

Funding information
National Science and Technology Major Project, Grant/Award Number: 2017ZX05035002-002

Abstract

Both of the coalbed methane (CBM) and shale gas reservoirs are dominated by nanometer-scale pores with their nanopore structures controlling the occurrence, enrichment, and accumulation of natural gas. Low-pressure nitrogen gas adsorption (LP-N_2GA), low-pressure carbon dioxide gas adsorption (LP-CO_2GA), high-pressure methane adsorption (HPMA), and field emission scanning electron microscope (FE-SEM) experiments were conducted on 14 different-rank coal samples and nine Longmaxi shale samples collected from various basins in China to compare their nanopore characteristics. The FE-SEM results indicate that the pore structures of both the coal and shale samples consist of nanometer-sized pores that primarily developed in the organic matter. The types of their isothermal adsorption curves are similar. However, the coal and shale samples possess various hysteresis loops, which suggest that the nanopores in shale are open-plated, whereas those in coal are semi-open. Furthermore, the specific surface area (SSA) and pore volume (PV) of the micropores in coal are much larger than those of the mesopores, with the micropore SSAs accounting for 99% of the total SSA in the coal samples. However, the micropore SSAs in the shale samples only account 42.24% of the total SSA. These different nanopore structures reflect their different methane adsorption mechanisms. The methane adsorption of coal is primarily controlled by the micropore SSA, whereas that of shale is primarily controlled by the mesopore SSA. If we use mesopore SSA to analyze its impact on methane adsorption capacity of coal and shale, it will be mismatched. However, no mismatching relationship exists between the total SSAs and adsorption capacities of coal and shale. This study highlights the controlling effect of total SSA on methane adsorption capacity.

KEYWORDS

adsorption capacity, CBM, nanopore structure, SEM, shale gas, specific surface area

1 | INTRODUCTION

Unconventional oil and gas exploration and development has undergone rapid growth over the past decade and has already induced a significant change in the global energy industry.[1-3] Two typical and important unconventional natural gas reservoirs, coalbed methane (CBM) and shale gas, are already being commercially developed in China.[4] A breakthrough in CBM development was made in early 2006, but there has only been a relatively slow increase in production since then due to a number of factors,[5] with 53.4×10^8 m^3 of CBM production in 2018. Shale gas production reached 108×10^8 m^3 in 2018, substantially exceeding that of CBM, although shale gas development began relatively later in China.[6]

Coalbed methane and shale gas reservoirs possess several similar features. (a) Both are "self-generation and self-storage" reservoirs,[4] meaning they can generate and store natural gas by themselves. (b) Both contain a certain amount of adsorbed gas.[7-10] The adsorbed gas content accounts for more than 80% of the total CBM gas content, and its saturated methane adsorption capacity can exceed 10 m^3/t.[7,8] However, the adsorbed gas content in shale only accounts for 30%-60% of the total gas content, with a saturated adsorption capacity that is usually in the 2-4 m^3/t range.[9,10] (c) Both are dual-pore media consisting of matrix pore and fracture.[11,12] The occurrence of free and adsorbed gases is controlled by the pore size, and gas transport is controlled by the fractures.[12,13] The predominantly nanometer-sized pores in coal and shale are much smaller than those in conventional sandstone and carbonate reservoirs,[14-18] with this nanopore structure controlling the occurrence, enrichment, and accumulation of natural gas in coal and shale.[19-21] Therefore, the characterization and quantitative analysis of nanopore systems are of great significance in evaluating the resource potential and development capability of CBM and shale gas reservoirs.[19-21]

The IUPAC classification of pores is divided into three main categories: micropores (<2 nm), mesopores (2-50 nm), and macropores (>50 nm).[22] Similar experimental methods are used in the pore structure characterization of coal and shale gas reservoirs,[23-28] which primarily consist of fluid injection and noninvasive imaging methods. The fluid injection method includes low-pressure nitrogen gas adsorption (LP-N_2GA),[24,25,28] low-pressure carbon dioxide gas adsorption (LP-CO_2GA),[7,11,29] high-pressure mercury injection (HPMI),[30,31] and low-field nuclear magnetic resonance (LF-NMR).[15,24,32] The noninvasive imaging method includes micro- and nano-CT,[26] scanning electron microscope (SEM),[28] focused ion beam scanning electron microscope (FIB-SEM),[12,33] and small-angle neutron scattering (SANS).[21] Each of these methods has been commonly employed to study their pore size distribution (PSD), specific surface area (SSA), pore volume (PV), and other nanopore structure characteristics.[23-28] However, few comparative studies have investigated the nanopore structure differences between coal and shale,[21,34] even though these differences are important in understanding their different gas storage mechanisms.

The methane adsorption capacity of coal is generally much larger than that of shale,[35-38] with the difference in nanopore structure being one of the key factors for this difference in adsorption capacity. The SSA of porous media, such as coal, shale, and activated carbon, is the key parameter that influences the adsorption capacity of the adsorbents.[13,29,39] A larger SSA means the medium can provide more adsorption sites, resulting in a higher adsorption capacity.[13] However, some studies[24,37-42] have shown that a mismatching relationship between the methane adsorption capacities and SSAs of coal and shale exists, where coal has a smaller SSA but a stronger adsorption capacity. For example, Li et al[24] indicated that the SSA of different-rank coal samples is in the 0.059-5.603 m^2/g range, Shan et al[38] demonstrated that vitrinite-rich coals have an average SSA of 2.429 m^2/g, and Tao et al[40] found that the SSA of low-rank coals is in the 0.19-5.6 m^2/g range, whereas many studies have shown that the SSA of the overmatured Longmaxi Formation shale can reach 10-30 m^2/g,[37,41,42] which is obviously larger than that of coal. Therefore, this mismatching relationship between the SSAs and adsorption capacities of coal and shale also needs to be reasonably explained.

The objective of this study is to elucidate the similarities and differences in the nanopore structure characteristics of coal and shale samples and better understand the occurrence mechanism of methane in these unconventional reservoirs. A comprehensive suite of fluid injection and noninvasive imaging experiments was conducted on different-rank coal and

TABLE 1 Basic properties of the coal samples used in this study

			Proximate analysis (wt.%)			
No.	Sample	$R_{o,m}$ (%)	M_{ad}	A_{ad}	V_{ad}	FC_{ad}
1	SM-8	0.56	3.37	3.63	25.32	67.68
2	SXBD3-4	0.84	1.68	6.32	13.27	78.73
3	M115-3	1.49	1.58	9.04	5.01	84.37
4	M115-5	1.53	2.32	7.54	7.60	82.54
5	M115-11	1.54	1.76	8.20	6.20	83.84
6	M115-34	1.64	1.65	9.15	6.21	82.99
7	M115-36	1.69	2.14	7.21	8.65	82
8	SM-1	1.83	2.56	8.23	9.12	80.09
9	M115-39	1.84	1.38	8.45	9.21	80.96
10	M115-40	1.93	1.65	7.27	7.64	83.44
11	M115-46	1.97	1.51	8.81	6.64	83.04
12	M115-53	1.94	1.52	6.84	8.41	83.23
13	WYM-1	2.52	1.74	8.56	6.84	82.86
14	N301	2.81	1.23	9.25	6.35	83.17

TABLE 2 Basic properties of the shale samples used in this study

No.	Sample	$R_{o,m}$ (%)	TOC (%)	Mineral composition (%)					
				Quartz	Plagioclase	Calcite	Dolomite	Pyrite	Clay
1	Y105-1	2.47	1.9	28.1	4.2	14.9	14.2	3.8	34.8
2	Y105-3	2.45	2.0	32.4	3.5	17.6	7.9	4.0	34.6
3	Y105-5	2.53	2.4	34.8	3.3	20.6	7.7	4.4	29.2
4	Y105-7	2.56	2.6	38.0	2.9	17.1	8.2	5.2	28.6
5	Y105-9	2.51	2.3	34.6	4.0	14.4	7.3	6.3	33.4
6	Y105-11	2.48	2.8	35.7	3.7	17.3	12.3	4.1	26.9
7	Y105-14	2.71	4.2	36.2	5.0	14.4	13.2	5.0	26.2
8	Y105-15	2.68	4.9	33.1	5.0	14.4	19.4	4.5	23.6
9	Y105-16	2.67	4.4	28.3	1.1	29.7	11.0	2.7	27.2

overmatured Longmaxi shale samples collected from several basins in China to evaluate their nanopore structure characteristics, which are particularly significant for evaluating CBM and shale gas reservoirs.

2 | SAMPLES AND EXPERIMENTS

2.1 | Samples

We selected 14 different-rank coal samples from several basins in China, including the Ordos Basin (SM-8, Shenmu Block; M115, Mizhi Block), Qinshui Basin Baode Block (SXBD3-4, SM-1, WYM-1), and Sichuan Basin Yibin Block (N301). The experimental results of the proximate analysis and maximum vitrinite reflectance ($R_{o,m}$) of the coal samples are shown in Table 1, with the $R_{o,m}$ distribution ranging from low rank (0.56%) to high rank (2.81%). The moisture (M_{ad}), ash (A_{ad}), volatile (V_{ad}), and fixed carbon (FC_{ad}) contents of the samples span 1.23%-3.37%, 3.63%-9.25%, 5.01%-25.32%, and 67.68%-84.37%, respectively.

Nine core samples were collected from the Lower Silurian Longmaxi Shale Formation in southern Sichuan Basin,[4] which is well known for its shale gas reserves in southern China, where the distribution of thick Paleozoic shales is the primary target region for shale gas exploration and development in China.[4] The $R_{o,m}$ distribution of these overmatured shale samples spans the 2.45%-2.71% range (Table 2). The total organic carbon (TOC) is between 1.9% and 4.9%, with a greater abundance of organic matter at the base of the Longmaxi Formation. The shale samples are primarily composed of quartz and clay minerals.

2.2 | FE-SEM analysis

The pore structure of the coal and shale samples was imaged using a FEI Helios 650 field emission scanning electron microscope (FE-SEM), with the secondary electron (SE) mode used for imaging (voltage: 10 kV, current: 0.4 nA, maximum resolution: 2 nm). The sample surface was polished with argon ions and then plated with carbon prior to the FE-SEM imaging. The purpose of argon ion polishing was to achieve a flat sample surface, and the purpose of carbon plating was to intensify the electrical conductivity of the sample.

2.3 | Low-pressure nitrogen gas adsorption (LP-N2GA)

A Micromeritics ASAP 2420 specific surface analyzer was used to conduct the LP-N_2GA experiments at 77 K. N_2 has a relatively low saturation vapor pressure (p_0) at this low temperature, which allows a broad range of N_2 adsorption and desorption isotherms to be obtained (p/p_0 = 0.0095-0.995, where p is the equilibrium pressure). The SSAs of coal and shale are generally calculated via the BET (Brunauer-Emmett-Teller) equation,[43] the original form of which is shown as Equation 1.

$$V_a = V_m \frac{cx}{1-x} \frac{1-(n+1)x^n + nx^{n+1}}{1+(c-1)x - cx^{n+1}} \quad (1)$$

where

$$x = p/p_0 \quad (2)$$

V_a is the total volume of adsorption, V_m is the volume of monolayer adsorption, c is a constant related to the heat of adsorption, p is the equilibrium pressure, p_0 is the saturation vapor pressure of N_2 at 77 K (0.1 MPa), n is the number of adsorption layers, and x is a variable associated with the pressure and heat of adsorption. If $n = \infty$, Equation (1) can be converted into the following BET equation with a frequently used form:

$$V_a = V_m \frac{cp}{(p_0 - p)\left[1 + (c-1)p/p_0\right]} \quad (3)$$

Equation (3) can be linearized to calculate V_m as:

$$\frac{p}{V_a(p_0-p)}=\frac{1}{V_mC}+\frac{C-1}{V_mC}\times\frac{p}{p_0} \quad (4)$$

where V_m can be obtained through the slope and intercept of the linear relationship between $p/[V_a(p_0-p)]$ and p/p_0 within the range of p/p_0 = 0.05-0.35. The SSA of a sample via the BET equation (S_{BET}) can then be calculated as:

$$S_{BET}=A_m\times N_A\times\frac{V_m}{22414}\times10^{-18} \quad (5)$$

where A_m is the cross-sectional area of hexagonal close-packed nitrogen molecules at 77 K (0.162 nm^2), and N_A is Avogadro's constant (6.022×10^{23}/mol). This simplifies Equation (5) to:

$$S_{BET}=4.352\times V_m \quad (6)$$

The SSAs calculated via the BET equation can represent the mesopore SSAs (meso-SSA, 2-50 nm) in this study since LP-N_2GA can only effectively characterize pores with pore size > 2 nm, and macropores (>50 nm) are not well developed in coal and shale.

2.4 | Low-pressure carbon dioxide gas adsorption (LP-CO2GA)

LP-CO_2GA experiments were also conducted using a Micromeritics ASAP 2420 specific surface analyzer at 273.15 K. The adsorption isotherms can only be obtained for p/p_0 = 0.00001-0.03 since CO_2 has a higher saturation vapor pressure. The Dubinin-Radushkevich (DR) equation,[44] which is based on micropore-filling theory, is primarily used to calculate the micropore SSAs from the LP-CO_2GA results as follows:

$$V_a=V_0\exp\left[-\left(\frac{RT\ln(p_0/p)}{\beta E_0}\right)^2\right] \quad (7)$$

where V_a is the adsorption capacity, V_0 is the micropore-filling adsorption capacity, R is the universal gas constant (8.314 J/mol/K), T is the absolute temperature (K), p is the experimental pressure (MPa), p_0 is the saturation vapor pressure of CO_2 at 273.15 K (3.48 MPa), β is a characteristic constant, and E_0 is the characteristic energy of adsorption. Equation (7) is usually linearized to calculate V_0 as:

$$\lg V_a=\lg V_0-D\left[\lg(p_0/p)\right]^2 \quad (8)$$

where

$$D=2.303\left(\frac{RT}{\beta E_0}\right)^2 \quad (9)$$

Then, the SSA of micropores based on DR equation is given by:

$$S_{DR}=A_m\times N_A\times\frac{V_0}{22414}\times10^{-18} \quad (10)$$

where A_m is the cross-sectional area of the CO_2 molecules at 273.15 K (0.170 nm^2), and N_A is the Avogadro's constant (6.022×10^{23}/mol). This simplifies Equation (10) to:

$$S_{DR}=4.566\times V_0 \quad (11)$$

The SSAs calculated via the DR equation can represent the micropore SSAs (micro-SSAs, <2 nm) in this study since LP-CO_2GA can only effectively characterize < 2 nm pores. The total SSA (S_{total}) of each sample can therefore be defined as:

$$S_{total}=S_{DR}+S_{BET} \quad (12)$$

2.5 | High-pressure methane adsorption (HPMA)

The HPMA experiments were carried out with a Rubotherm gravimetric adsorption instrument. The core component of the instrument is the magnetic suspension balance, which possesses a 10μg precision. The maximum test temperature and pressure are 150°C and 35 MPa, respectively, and the long-term temperature fluctuation range can be controlled with ± 0.2°C. First, each sample was crushed, and 150-380 μm (40-100 mesh) particles were then selected and dried in an oven at 105°C for 24 h. Prior to the experiments, the samples were vacuum-degassed for 4 h at 150°C to remove any moisture and impurities. The HPMA experiments on the coal and shale samples were tested at 60°C after blank and buoyancy experiments were performed. The excess adsorption capacity (m_{ex}) measured at each equilibrium pressure point can be expressed as follows[37]:

$$m_{ex}=\Delta m-m_{sc}-m_s+(V_{sc}+V_s)\times\rho_g \quad (13)$$

where Δm is the balance reading, m_{sc} is the mass of the sample container, m_s is the mass of the sample, V_{sc} is the volume of the sample container, V_s is the volume of the sample, and ρ_g is the bulk gas density. An evaluation of the real adsorption capacity of each sample requires the conversion of m_{ex} to the absolute absorption capacity (m_{abs}) via the determination of adsorbed-phase density (ρ_a) as:

$$m_{abs}=m_{ex}/(1-\rho_g/\rho_a) \quad (14)$$

3 | RESULTS

3.1 | Mesopore characteristics

The LP-N_2GA results of the representative coal and shale samples are shown in Figure 1, with the adsorption curves

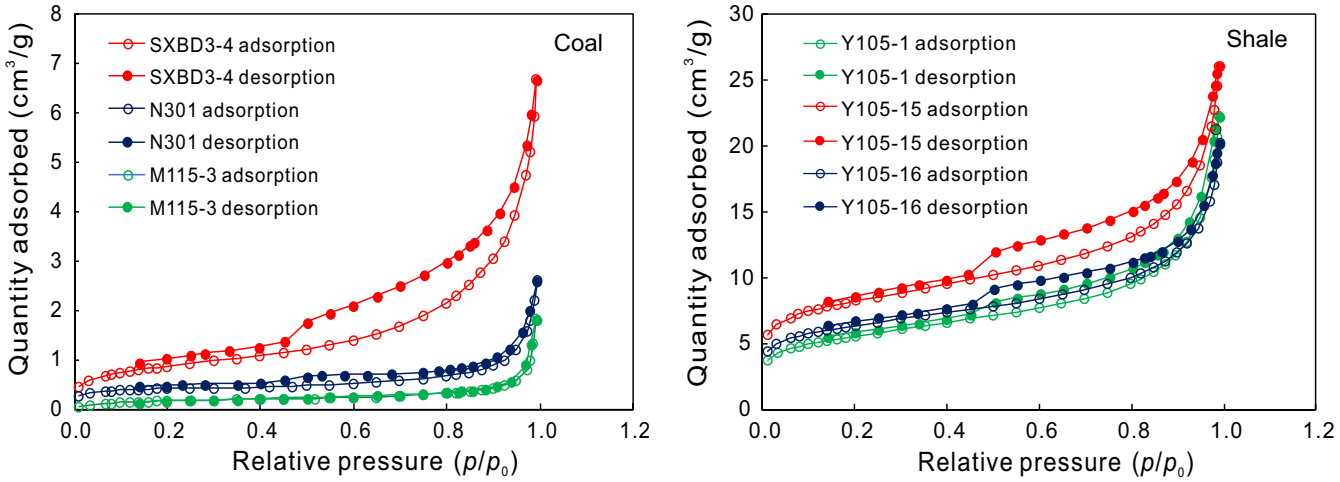

FIGURE 1 LP-N_2GA isotherms of representative coal and shale samples

of coal and shale exhibiting similar characteristics. IUPAC classification indicates that these curves are representative of type II adsorption isotherms,[45] with the adsorption curves rising slowly at low pressures ($0 < p/p_0 < 0.05$) and increasing linearly within a certain pressure range ($0.05 < p/p_0 < 0.35$). The adsorption curves then increase sharply and are still unsaturated, even when p is close to p_0, with nitrogen gas becoming condensed in the pores. The adsorption isotherm does not coincide with the desorption isotherm at relatively high pressures ($p/p_0 > 0.4$), forming a hysteresis loop, with the shape of the hysteresis loop reflecting the pore structure in the adsorbent.[45] The shape of the hysteresis loop is basically the same for all the shale samples, as shown in Figure 1. This shape is most similar to a type H3 hysteresis loop according to the IUPAC classifications,[45] reflecting open parallel plate pores with good connectivity, which is a favorable pore structure for gas migration. However, the hysteresis loops for coal are different. For example, the desorption and adsorption curves for Samples N301 and M115-3 almost coincide with each other, reflecting the development of semi-open pores in the coal samples, which are favorable for gas adsorption but unfavorable for gas flow.

The BJH Equation [45] was used to calculate the mesopore volume and pore size distribution of coal and shale samples from the LP-N_2GA results, as shown in Figure 2. The nitrogen adsorption capacity of shale is much larger than that of coal, which is reflected by the much larger mesopore volumes in the shale samples. The average mesopore volume is 0.033 cm^3/g in the shales (0.027-0.035 cm^3/g range), whereas the average mesopore volume is 0.0031 cm^3/g in the coals (0.001-0.010 cm^3/g range). However, the PSD of the coal and shale samples is approximately the same. A certain number of 2-100 nm pores developed in both the coal and shale samples. It is worth noting that a false peak will appear at the approximately 4 nm pore size when using the BJH equation for desorption curve analysis due to the tensile strength effect (TSE),[46] which is closely correlated with the hysteresis of the desorption curve. This false peak does not exist in Sample

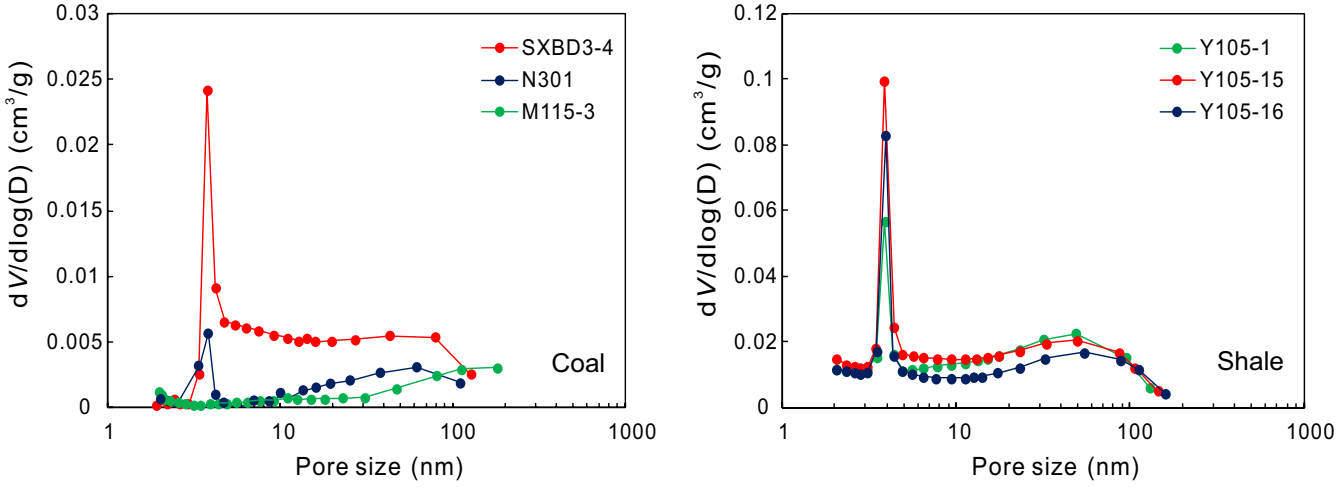

FIGURE 2 Pore size distribution of representative coal and shale samples based on the BJH equation

M115-3 since its adsorption and desorption curves almost coincide with each other.

The best fit to the LP-N_2GA data for each sample is determined via Equation (4) to calculate the meso-SSAs of the coal and shale samples, as shown in Figure 3. A clear linear relationship exists for $0.05 < p/p_0 < 0.30$, satisfying the BET equation. The sum of the slopes and intercepts of the best-fit lines for the coal samples is larger, indicating that the monolayer adsorption capacity is smaller. This results in a much smaller meso-SSA for coal than that for shale. The average meso-SSA for the coal samples is 1.01 m^2/g (0.27-3.12 m^2/g range), whereas the average meso-SSA for the shale samples is 22.46 m^2/g (19.30-28.20 m^2/g range).

3.2 | Micropore characteristics

Figure 4 shows the LP-CO_2GA isotherms of the coal and shale samples, which exhibit similar characteristics. Their CO_2 adsorption capacity increases steadily with increasing pressure. This curvature is indicative of a type I adsorption isotherm according to the IUPAC classifications.[45] The curve characteristics are different from those in the aforementioned N_2 adsorption experiment due to the narrow pressure range of the CO_2 adsorption experiment ($p/p_0 < 0.03$). Furthermore, the CO_2 adsorption capacity of coal is much larger than that of shale, which indicates more developed micropores in coal.

The DFT equation was applied to calculate the PV and PSD of the micropores in coal and shale from the LP-CO_2GA results, as shown in Figure 5. The micropore volume of shale is much smaller than that of coal, with an average value of 0.0066 cm^3/g, whereas the average micropore volume of coal is 0.0598 cm^3/g. However, the micropore size distribution of coal and shale is roughly the same, with most pore sizes in the 0.5-1.0 nm range.

Similarly, all the LP-CO_2GA data are linear-fitted to calculate the micro-SSA of the coal and shale samples based on Equation (8), as shown in Figure 6. Excellent fits are obtained via the DR equation, as indicated by the high correlation coefficients ($R^2 > 0.99$), which are similar to the LP-N_2GA results obtained via the BET equation. The intercepts of the linear fits for coal are relatively larger than those for shale, which indicates that coal has a larger micropore-filling adsorption capacity and higher micro-SSA than shale. The micro-SSA of the coal samples is 24.45-221.93 m^2/g, with an average of 159.23 m^2/g, while the micro-SSA of the shale samples is 11.48-22.74 m^2/g, with an average of 16.59 m^2/g.

3.3 | Methane adsorption characteristics

The measured excess adsorption isotherms of the samples are presented in Figure 7, where the excess adsorption capacity increases with increasing pressure until it reaches a maximum value at approximately 10 MPa and then begins to decrease with increasing pressure. This observed trend conforms to the adsorption characteristics of a supercritical fluid[47] and is completely different from the characteristics of the aforementioned LP-N_2GA and LP-CO_2GA curves. The main reason is that both the LP-N_2GA and LP-CO_2GA belong to subcritical adsorption, whereas the methane adsorption belongs to supercritical adsorption. The critical temperature of methane, nitrogen, and carbon dioxide is −82.5°C, −146.9°C, and 31°C, respectively. When the temperature of adsorption experiment is higher than its critical temperature, no matter how much pressure is applied, it will not liquefy. We call this phenomenon as supercritical adsorption and vice versa as subcritical adsorption. These two types of adsorption are naturally different.

The volume of the adsorbed phase cannot be ignored for supercritical adsorption, and the measured adsorption capacity is the excess adsorption capacity, which cannot reflect the real adsorption capacity of the adsorbent unless it is converted to the absolute adsorption capacity.[37]

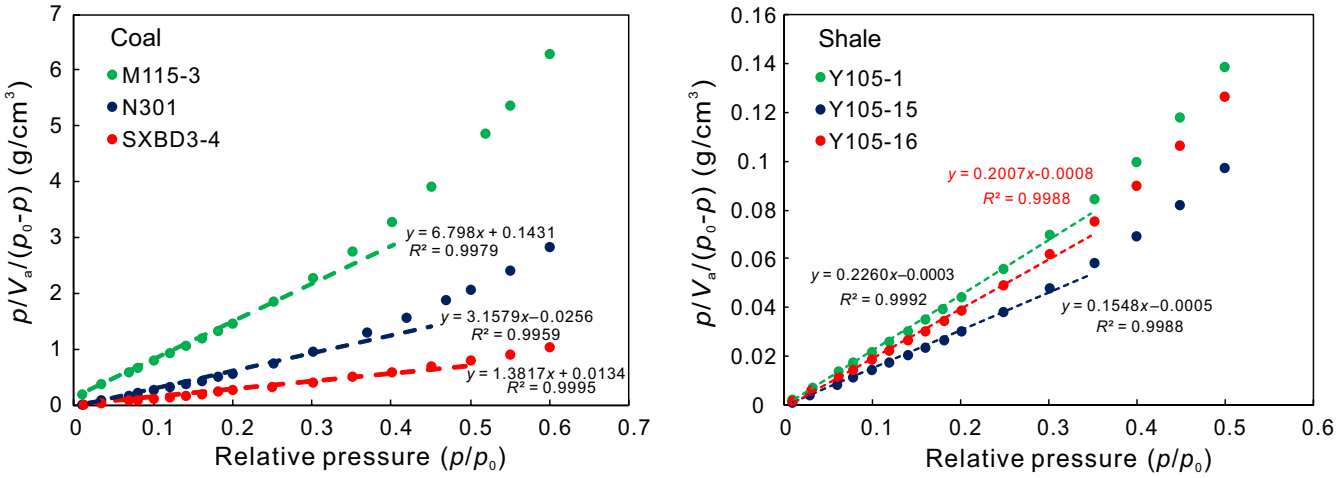

FIGURE 3 Linear fitting results of the LP-N_2GA data for representative coal and shale samples via the BET equation

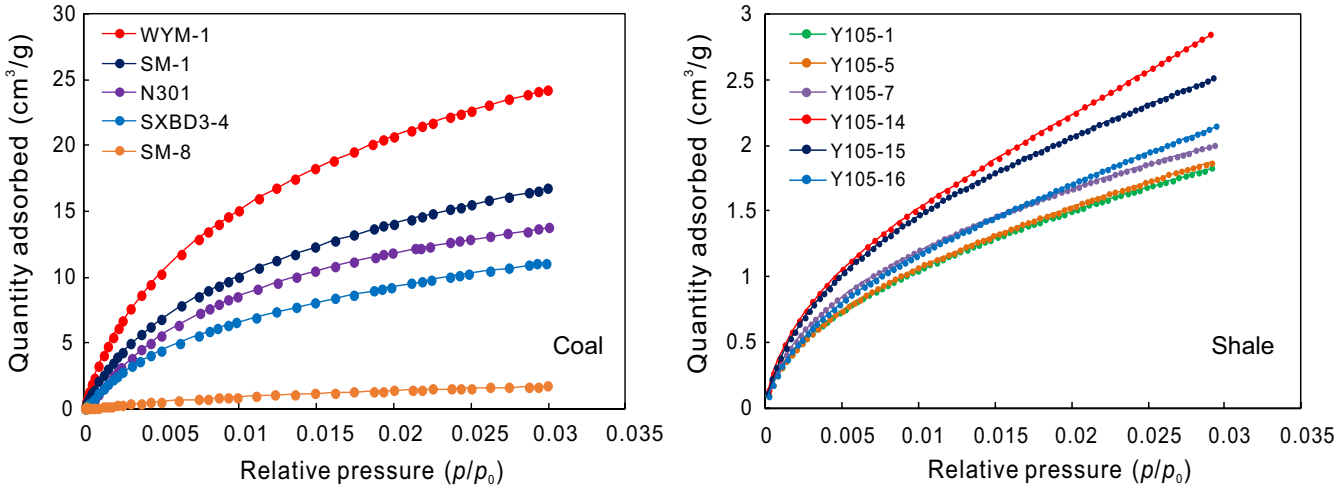

FIGURE 4 LP-CO_2GA isotherms of representative coal and shale samples

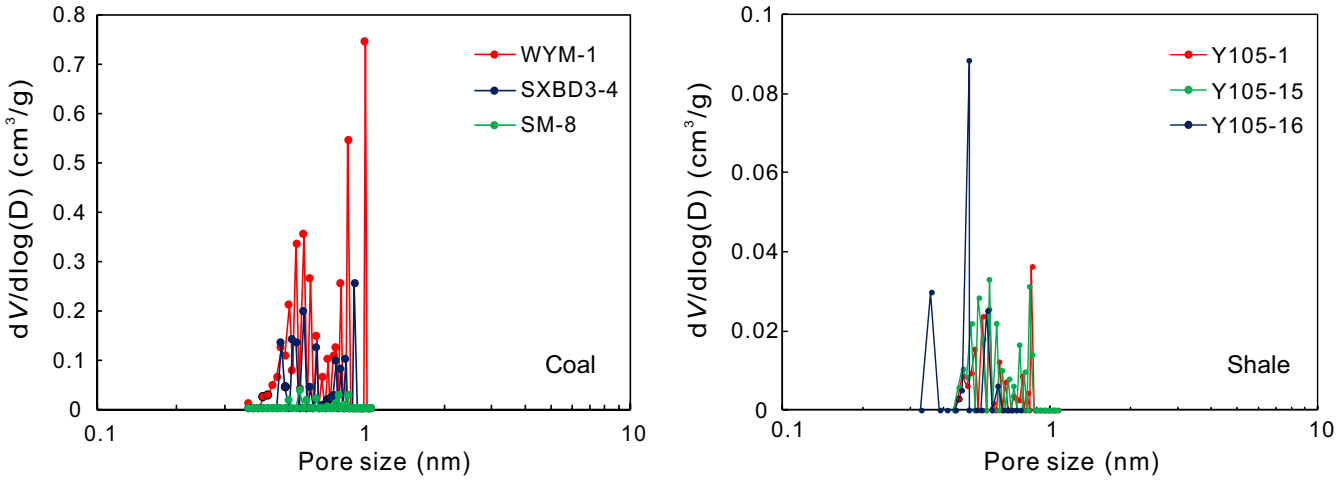

FIGURE 5 Pore size distribution of representative coal and shale samples based on the DFT equation

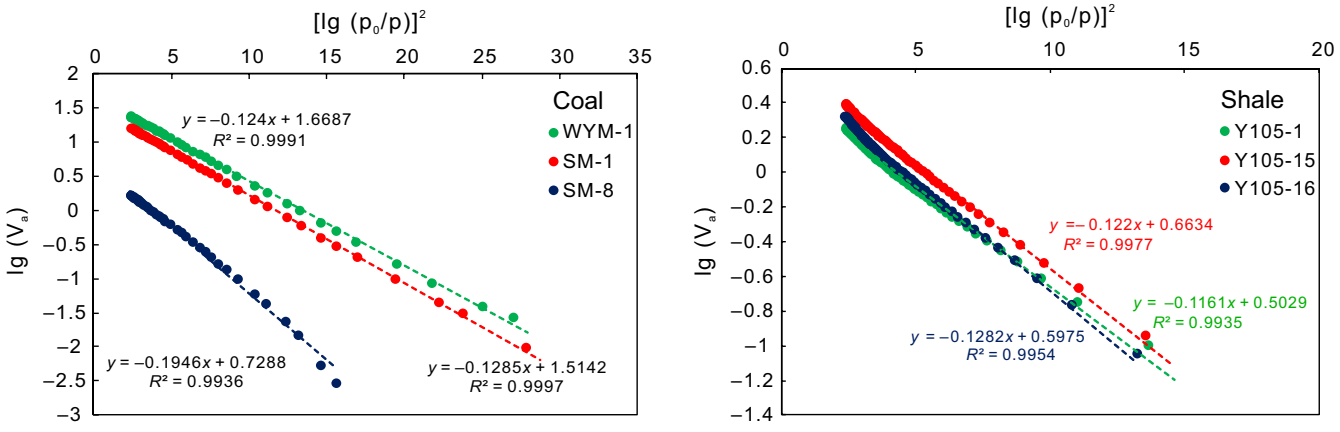

FIGURE 6 Linear fitting of the LP-CO_2GA data for representative coal and shale samples by the DR equation

Current conversion methods differ considerably in the literature.[35,37] Here, the maximum excess adsorption capacity, as opposed to the absolute adsorption capacity, is used to compare the adsorption capacities of coal and shale, which avoids the problems due to different conversion parameters. Figure 7 shows that the maximum adsorption capacity

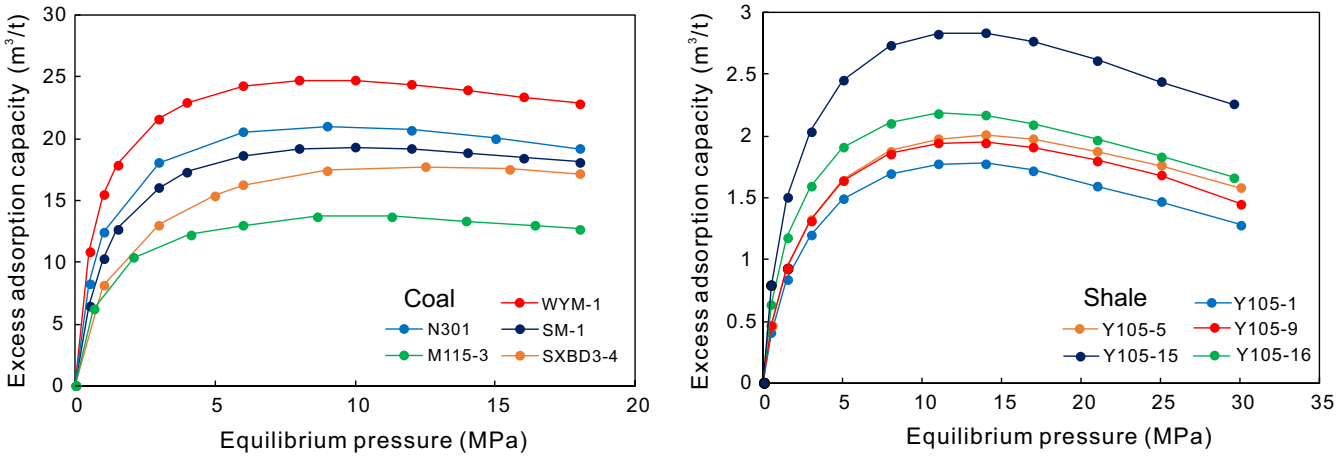

FIGURE 7 High-pressure methane adsorption isotherms of representative coal and shale samples

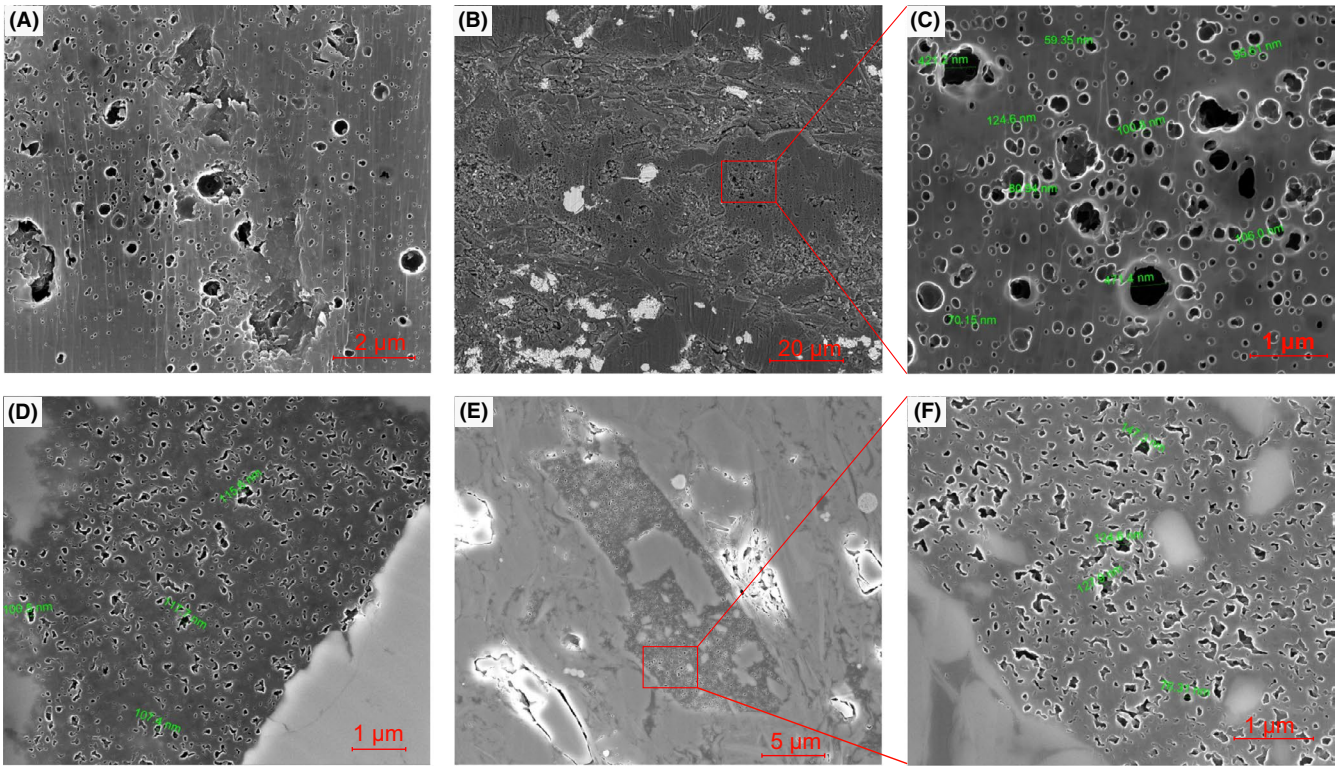

FIGURE 8 FE-SEM images of the organic and inorganic pores in selected coal and shale samples. A, B, C-SXBD3-4, coal, $R_{o,m} = 0.84\%$; D-Y105-1, shale, $R_{o,m} = 2.47\%$; E, F-Y105-15, shale, $R_{o,m} = 2.68\%$

of the coal samples is much higher than that of the shale samples.

3.4 | SEM images

Representative SEM images of the coal and shale samples are shown in Figure 8. The pores in the coal and shale samples are well developed in the organic matter due to hydrocarbon generation. The abundant organic pores suggest that a great amount of gas had been generated during the evolution of organic matter. However, the pore shape of coal and shale samples is different with circular shape and irregular shape, respectively (Figure 8C,F). It shows that shale in this area has undergone pressure compaction and pore deformation after gas generation. Unlike coal, many inorganic pores can be developed in shales due to diagenesis (Figure 8E).

The organic matter pores account for a large proportion of their respective pore structures and are generated when the coal or shale reaches a certain thermal evolution range. These pores are highly influenced by the organic carbon

content and maturity of the organic matter and will increase with increasing organic carbon content and maturity. However, the micropores and SSA begin to decrease after the organic matter reaches a certain maturity (universally acknowledged as $R_o > 2.4\%$).[48,49] The lipophilic property of the organic matter makes the organic matter nanopores an important storage space for the absorbed gas. The gas is primarily stored on the pore surface in an absorbed state when the organic matter pores are relatively small, whereas the absorbed gas is stored on the pore surface when the organic matter pores are relatively large, with the free gas stored in the pore centers.

4 | DISCUSSION

4.1 | Relationship between SSA and methane adsorption capacity

The adsorption capacity of porous media is mainly controlled by the SSA.[11,13] As two special porous media, both coal and shale should meet this law. However, many studies have indicated that a mismatching relationship exists between the methane adsorption capacity and SSA of coal and shale; that is, shale has a larger SSA but lower adsorption capacity (Figure 9). This illogical mismatching relationship is due to the SSA in those references only tested by LP-N_2GA experiments,[38,40] which cannot represent the true SSAs of the coal and shale samples. Figure 9 illustrates this illogical mismatching relationship, which indicates that shales have a relatively large BET SSA but a much smaller adsorption capacity. Here, LP-N_2GA and LP-CO_2GA experiments are combined to analyze the different controlling factors of the adsorption capacity of coal and shale. The meso-SSA of coal exhibits no correlation with its methane adsorption capacity (Figure 10A), whereas the micro-SSA of coal exhibits a strong positive correlation with its methane adsorption capacity (Figure 10B), which indicates that its methane adsorption capacity is primarily controlled by its micro-SSA. The meso-SSA of shale exhibits a better correlation with the methane adsorption capacity than the micro-SSA of shale (Figure 10C,D), which indicates that the methane adsorption capacity of shale is primarily controlled by its meso-SSA. This proves that the controlling mechanism of the adsorption capacities of coal and shale is completely different.

While considering the relationship between the total SSA and methane adsorption capacity, Figure 11 shows a completely different relationship with that shown in Figure 9. The adsorption capacity in this study presents a strong positive correlation with total SSA (Figure 11), which indicates that the methane adsorption capacity is controlled by the total SSA for both coal and shale, and highlights that no mismatching relationship exists between the SSAs and adsorption capacities of coal and shale.

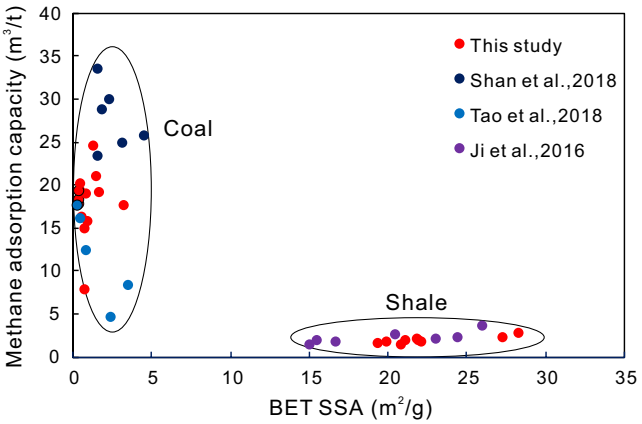

FIGURE 9 A mismatching relationship between the BET SSAs and methane adsorption capacities of coal and shale. Some data are cited from published articles[38,40,41]

4.2 | Comparison of coal and shale nanopore structure characteristics

To quantitatively characterize the nanopore structure of coal and shale, LP-N_2GA is preferred and commonly used, whereas LP-CO_2GA is rarely applied.[13-15,24-26] While the molecular diameter of nitrogen is almost equal to that of carbon dioxide (N_2: 0.36 nm, CO_2: 0.33 nm), the different experimental temperatures are the major reason for the different detectable pore size ranges when using nitrogen and carbon dioxide as the adsorbate. Thomas and Damberger[50] have indicated that the diffusion rate of carbon dioxide at 273.15 K is 10^5 times greater than that of nitrogen at 77 K, with this significant increase in the gas diffusion rate due to the increased analysis temperature. This relatively high thermal energy enables the carbon dioxide molecules to enter the micropores, resulting in micropore detection. The detectable pore size range of the two adsorption experiments is therefore completely different. The nitrogen adsorption experiment is only applicable for mesopore structure analysis and is recommended for calculating the meso-SSA via the BET equation, which is based on multilayer adsorption theory. Conversely, the carbon dioxide adsorption experiment is applicable for micropore structure analysis and is recommended for calculating the micro-SSA via the DR equation, which is based on micropore-filling theory.

The micro-SSAs of the coal samples are much larger than the meso-SSAs, accounting for 97.38%-99.87% of the total SSA, with an average of 99.28% (Table 3). It indicates that most pores in coal are closed for nitrogen under 77 K, but are accessible for carbon dioxide under 273.15 K. However, the micro-SSAs of the shale samples are smaller than the meso-SSAs, accounting for 36.71%-45.53% of the total SSA, with an average of 42.24%. These observations indicate that the nanopore structure of coal is totally different from that of shale. Micropores are mainly developed

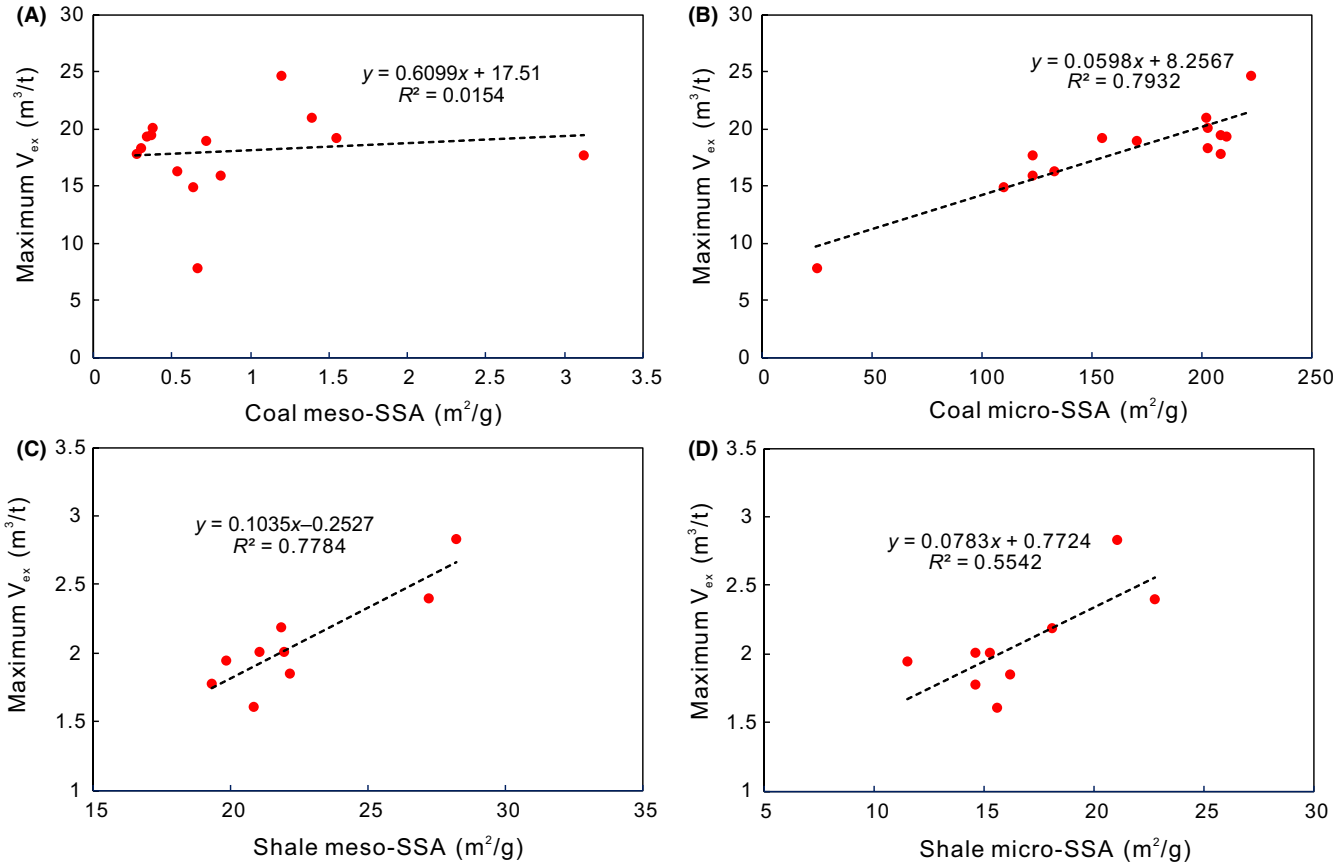

FIGURE 10 Relationship between the meso-/micro-SSAs and maximum excess adsorption capacities: coal (A, B) and shale (C, D). The maximum V_{ex} in the *y*-axis refers to the peak value of the excess adsorption capacity in the adsorption curves

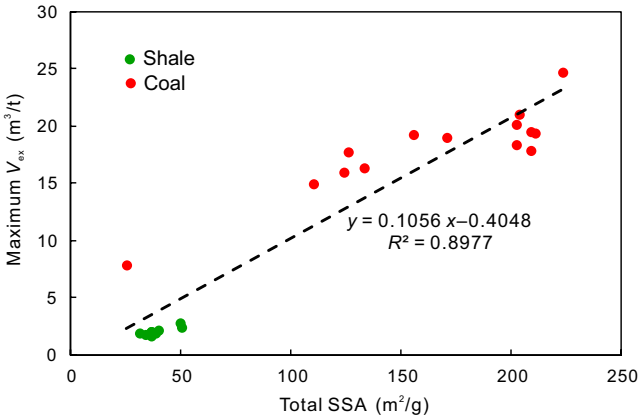

FIGURE 11 Relationship between the total SSAs and maximum excess adsorption capacities (V_{ex}) of coal and shale samples in this study

in the coal, with a large SSA, in favor of the storage of adsorbed gas. However, mesopores are mainly developed in the shale, with a relatively large volume, in favor of the storage of free gas.

As two typical unconventional natural gas reservoirs, CBM and shale gas reservoirs, possess some similar pore development characteristics, however, they also exhibit many micropore structure differences. More than 99% of the SSA in coal is provided by micropores, whereas micropores account for less than 50% of the total SSA in shale. Furthermore, the total SSA of coal is much larger than that of shale, which shapes the huge difference in the adsorption capacities of coal and shale. This study highlights the importance of conducting a comprehensive analysis of LP-N_2GA and LP-CO_2GA experiments to investigate the nanopore structure characteristics of coal and shale reservoirs, which are of particular significance for the micropore analysis of coal.

4.3 | Controlling factors for their different nanopore structure

As discussed above, the nanopore structure of coal and shale is completely different. In this section, we will briefly analyze its reasons and controlling factors for their difference in SSA and PV of nanopores. The difference in sedimentary microfacies between CBM and shale gas reservoir makes the difference in organic matter content and mineral matter content between them, which is the basic reason for the pore structure difference.

Unlike shale, the basic structural unit of coal is graphite-like microcrystalline formed by the superposition of

TABLE 3 SSA, PV, and methane adsorption capacity of all the coal and shale samples based on LP-N_2GA, LP-CO_2GA, and HPMA adsorption experiments

		N_2 adsorption		CO_2 adsorption		CH_4 adsorption		
Rock type	Sample	BET SSA (m^2/g)	BJH PV (cm^3/g)	DR SSA (m^2/g)	DR PV (cm^3/g)	maximum value of V_{ex} (m^3/t)	[a]Micro-SSA contribution rate (%)	[b]Micro-PV contribution rate (%)
Coal	SM-8	0.659	0.001477	24.45	0.00530	7.92	97.38	78.20
	SXBD3-4	3.120	0.010483	122.48	0.03076	17.75	97.52	74.58
	M115-3	0.627	0.002815	109.47	0.04393	15.01	99.43	93.98
	M115-5	0.809	0.003405	122.85	0.04930	15.97	99.35	93.54
	M115-11	0.529	0.001227	132.56	0.05320	16.40	99.60	97.75
	M115-34	0.266	0.001103	208.53	0.08368	17.90	99.87	98.70
	M115-36	0.299	0.001051	202.19	0.08114	18.41	99.85	98.72
	SM-1	1.545	0.004451	154.21	0.06179	19.30	99.01	93.28
	M115-39	0.714	0.003326	170.20	0.06830	19.07	99.58	95.36
	M115-40	0.362	0.001885	208.41	0.08364	19.46	99.83	97.80
	M115-46	0.338	0.001983	210.60	0.08451	19.43	99.84	97.71
	M115-53	0.374	0.001384	202.06	0.08109	20.20	99.82	98.32
	WYM-1	1.194	0.003089	221.93	0.08501	24.73	99.47	96.49
	N301	1.385	0.003693	201.94	0.03777	21.04	99.32	91.09
Shale	Y105-1	19.30	0.03160	14.54	0.00583	1.78	42.96	15.58
	Y105-3	20.80	0.03270	15.54	0.00624	1.61	42.76	16.01
	Y105-5	21.00	0.03260	15.25	0.00612	2.01	42.08	15.81
	Y105-7	22.10	0.03400	16.12	0.00647	1.86	42.18	15.98
	Y105-9	19.80	0.03300	11.48	0.00461	1.95	36.71	12.25
	Y105-11	21.90	0.03400	14.55	0.00584	2.01	39.91	14.65
	Y105-14	27.20	0.03350	22.74	0.00912	2.40	45.53	21.40
	Y105-15	28.20	0.03490	21.04	0.00844	2.84	42.72	19.48
	Y105-16	21.80	0.02690	18.07	0.00725	2.19	45.33	21.24

[a]Micro-SSA contribution rate (%) = micro-SSA/(micro-SSA + meso-SSA) × 100%.
[b]Micro-PV contribution rate (%) = micro-PV/(micro-PV + meso-PV) × 100%.

aromatic rings. Fryer[51] studied the activation of anthracite activated carbon by water vapor and found that the spacing of microcrystalline lamellae is only 0.7 nm, which constituted micropores in coal, that is, the so-called interlaminar pores. The micropore of coal is closely related to the microcrystalline structure of coal. In addition, the aromatic layers in coal are not arranged in an orderly manner, and there are dislocations between the aromatic layers. The disorderly accumulation of aromatic layers may be main cause for the formation of micropores with different shapes and sizes in coal.[52] This type of pores of aromatic layers is more developed in coals, leading to its larger micropore SSA and PV.

Nanopores in shale are mainly developed due to hydrocarbon generation. These pores are mainly micropores and mesopores. With the evolution of organic matter, the natural gas content gradually increases, which makes the micropores and mesopores to become the main storage space of shale. At the same time, many inorganic pores in shale developed due to diagenesis are always belong to mesopores. Therefore, the ratio of micropore SSA and PV of shale is much less than coal.

5 | CONCLUSION

A series of experimental methods, including LP-N_2GA, LP-CO_2GA, HPMA, and FE-SEM, have been conducted to comprehensively analyze and compare the nanopore structure characteristics in coal and shale. The main conclusions are as follows:

1. Nanopore structures are observed in the organic matter of both the coal and shale samples, and their adsorption curves exhibit similar characteristics. However, the hysteresis loops of coal and shale are different. The shale nanopores are always open and parallel-plated, with good connectivity, whereas the coal nanopores are semi-opened, with poor connectivity.
2. More than 99% of the SSA in coal is provided by micropores, whereas it is less than 50% in shale, which indicates that coal and shale have quite different nanopore structures. Coal has a predominant micropore structure, with a large SSA, that favors the storage of adsorbed gas. However, shale has a predominant mesopore structure, with a relatively large volume, that favors the storage of free gas.
3. The controlling mechanism for the adsorption capacities of coal and shale is completely different. The methane adsorption capacity of coal is primarily controlled by its micro-SSA, whereas that of shale is primarily controlled by its meso-SSA. Furthermore, no mismatching relationship exists between the total SSAs and adsorption capacities of coal and shale.
4. The SSA and PV of pores in coal are mainly provided by micropores of aromatic lamellae, while those in shale are mainly provided by mesopores developed during gas generation.

ACKNOWLEDGMENTS

This study was funded by the National Science and Technology Major Project (No. 2017ZX05035002-002).

ORCID

Shangwen Zhou https://orcid.org/0000-0003-0426-9683

REFERENCES

1. Curtis JB. Fractured shale-gas systems. *AAPG Bull*. 2002;86(11):1921-1938.
2. Montgomery SL, Jarvie DM, Bowker KA, Pollastro RM. Mississippian Barnett Shale, Fort Worth basin, north-central Texas: gas-shale play with multi-trillion cubic foot potential. *AAPG Bull*. 2005;89(2):155-175.
3. EIA. 2017. http://www.eia.gov/dnav/ng/ng_prod_sum_dcu_NUS_a.htm (accessed December 31, 2017).
4. Zou C, Zhang G, Yang Z, et al. Geological concepts, characteristics, resource potential and key techniques of unconventional hydrocarbon: on unconventional petroleum geology. *Petrol Expl Develop*. 2013;40(4):385-399.
5. Mu F, Wang H, Wu J, Sun B. Practice of and suggestions on CBM development in China. *Nat Gas Ind*. 2018;8(9):55-60. (In Chinese with English abstract).
6. Zou C, Dong D, Wang Y, et al. Shale gas in China: characteristics, challenges and prospects (II). *Petrol Expl Develop*. 2015;42(6):753-767.
7. Yin T, Liu D, Cai Y, Zhou Y. Methane adsorption constrained by pore structure in high-rank coals using FESEM, CO_2 adsorption, and NMRC techniques. *Energy Sci Eng*. 2019;00:1-17.
8. Zhang M, Fu X. Characterization of pore structure and its impact on methane adsorption capacity for semi-anthracite in Shizhuangnan Block, Qinshui Basin. *J Nat Gas Sci Eng*. 2018;60:49-62.
9. Tang X, Ripepi N, Stadie NP, Yu L, Hall MR. A dual-site Langmuir equation for accurate estimation of high pressure deep shale gas resources. *Fuel*. 2016;185:10-17.
10. Sakurovs R, Day S, Weir S, Duffy G. Application of a modified Dubinin-Radushkevich equation to adsorption of gases by coals under supercritical conditions. *Energy Fuels*. 2007;21(2):992-997.
11. Chen S, Tao S, Tang D, et al. Pore structure characterization of different rank coals using N_2 and CO_2 adsorption and its effect on CH_4 adsorption capacity: a case in Panguan Syncline, Western Guizhou, China. *Energy Fuels*. 2017;31(6):6034-6044.
12. Zhou S, Yan G, Xue H, Guo W, Li X. 2D and 3D nanopore characterization of gas shale in Longmaxi formation based on FIB-SEM. *Mar Pet Geol*. 2016;73:174-180.
13. Nie B, Liu X, Yang L, Meng J, Li X. Pore structure characterization of different rank coals using gas adsorption and scanning electron microscopy. *Fuel*. 2015;158:908-917.

14. Li X, Kang Y, Haghighi M. Investigation of pore size distributions of coals with different structures by nuclear magnetic resonance (NMR) and mercury intrusion porosimetry (MIP). *Measurement*. 2018;116:122-128.
15. Zheng S, Yao Y, Liu D, Cai Y, Liu Y. Characterizations of full-scale pore size distribution, porosity and permeability of coals: a novel methodology by nuclear magnetic resonance and fractal analysis theory. *Int J Coal Geol*. 2018;196:148-158.
16. Jiao K, Yao S, Liu C, et al. The characterization and quantitative analysis of nanopores in unconventional gas reservoirs utilizing FESE-FIB and image processing: an example from the lower Silurian Long-maxi Shale, upper Yangtze region, China. *Int. J. Coal Geol*. 2014;128:1-11.
17. Milliken KL, Rudnicki M, Awwiller DN, Zhang T. Organic matter-hosted pore system, Marcellus formation (Devonian), Pennsylvania. *AAPG Bull*. 2013;97:177-200.
18. Nelson PH. Pore throat sizes in sandstones, tight sandstones, and shales. *AAPG Bull*. 2009;93:1-13.
19. Loucks RG, Reed RM, Ruppel SC, Jarvie DM. Morphology, genesis, and distribution of nanometer-scale pores in siliceous mudstones of the Mississippian Barnett Shale. *J Sediment Res*. 2009;79:848-865.
20. Ross D, Bustin RM. Characterizing the shale gas resource potential of Devonian-Mississippian strata in the Western Canada Sedimentary Basin: application of an integrated formation evaluation. *AAPG Bull*. 2008;92:87-125.
21. Mastalerz M, He L, Melnichenko YB, Rupp JA. Porosity of coal and shale: insights from gas adsorption and SANS/USANS techniques. *Energy Fuels*. 2012;26:5109-5120.
22. International Union of Pure and Applied Chemistry. Manual of symbols and terminology. *Pure Appl Chem*. 1972;31:578.
23. Zhou S, Liu D, Cai Y, Yao Y, Li Z. 3D characterization and quantitative evaluation of pore-fracture networks of two Chinese coals using FIB-SEM tomography. *Int J Coal Geol*. 2017;174:41-54.
24. Li Y, Zhang C, Tang D, et al. Coal pore size distributions controlled by the coalification process: an experimental study of coals from the Junggar, Ordos and Qinshui basins in China. *Fuel*. 2017;206:352-363.
25. Fu H, Tang D, Xu T, et al. Characteristics of pore structure and fractal dimension of low-rank coal: a case study of Lower Jurassic Xishanyao coal in the southern Junggar Basin, NW China. *Fuel*. 2017;193:254-264.
26. Zhao Y, Sun Y, Liu S, Chen Z, Yuan L. Pore structure characterization of coal by synchrotron radiation nano-CT. *Fuel*. 2018;215:102-110.
27. Ross D, Bustin RM. The importance of shale composition and pore structure upon gas storage potential of shale gas reservoirs. *Mar Pet Geol*. 2009;26:916-927.
28. Tian H, Pan L, Xiao X, Wilkins R, Meng Z, Huang B. A preliminary study on the pore characterization of Lower Silurian black shales in the Chuandong Thrust Fold Belt, southwestern China using low pressure N_2 adsorption and FE-SEM methods. *Mar Pet Geol*. 2013;48:8-19.
29. Zhao J, Xu H, Tang D, Mathews JP, Li S, Tao S. A comparative evaluation of coal specific surface area by CO_2 and N_2 adsorption and its influence on CH_4 adsorption capacity at different pore sizes. *Fuel*. 2016;183:420-431.
30. Yao Y, Liu D, Tang D, et al. Fractal characterization of seepage-pores of coals from China: an investigation on permeability of coals. *Comput Geosci*. 2009;35(6):1159-1166.
31. Clarkson CR, Solano N, Bustin RM, et al. Pore structure characterization of North American shale gas reservoirs using USANS/SANS, gas adsorption, and mercury intrusion. *Fuel*. 2013;103:606-616.
32. Lyu C, Ning Z, Wang Q, Chen M. Application of NMR T_2 to pore size distribution and movable fluid distribution in tight sandstones. *Energy Fuels*. 2018;32(2):1395-1405.
33. Li Z, Liu D, Cai Y, Ranjith PG, Yao Y. Multi-scale quantitative characterization of 3-D pore-fracture networks in bituminous and anthracite coals using FIB-SEM tomography and X-ray μ-CT. *Fuel*. 2017;209:43-53.
34. Firouzi M, Rupp EC, Liu CW, Wilcox J. Molecular simulation and experimental characterization of the nanoporous structures of coal and gas shale. *Int J Coal Geol*. 2014;121:123-128.
35. Tian H, Li T, Zhang T, Xiao X. Characterization of methane adsorption on overmature Lower Silurian-Upper Ordovician shales in Sichuan Basin, Southwest China: experimental results and geological implications. *Int J Coal Geol*. 2016;156:36-49.
36. Gasparik M, Ghanizadeh A, Bertier P, Gensterblum Y, Bouw S, Krooss BM. High-pressure methane sorption isotherms of black shales from the Netherlands. *Energy Fuels*. 2012;26:4995-5004.
37. Zhou S, Xue H, Ning Y, Guo W, Zhang Q. Experimental study of supercritical methane adsorption in Longmaxi shale: Insights into the density of adsorbed methane. *Fuel*. 2018;211:140-148.
38. Shan C, Zhang T, Liang X, et al. On the fundamental difference of adsorption-pores systems between vitrinite- and inertinite-rich anthracite derived from the southern Sichuan basin, China. *J Nat Gas Sci Eng*. 2018;3:32-44.
39. Okolo GN, Everson RC, Neomagus H, Roberts MJ, Sakurovs R. Comparing the porosity and surface areas of coal as measured by gas adsorption, mercury intrusion and SAXS techniques. *Fuel*. 2015;141:293-304.
40. Tao S, Chen S, Tang D, Zhao X, Xu H, Li S. Material composition, pore structure and adsorption capacity of low-rank coals around the first coalification jump: a case of eastern Junggar Basin, China. *Fuel*. 2018;211(29):804-815.
41. Ji W, Song Y, Jiang Z, Meng M, Liu Q, Chen L. Fractal characteristics of nano-pores in the Lower Silurian Longmaxi shales from the Upper Yangtze Platform, south China. *Mar Pet Geol*. 2016;78:88-98.
42. Tian H, Pan L, Zhang T, Xiao X, Meng Z, Huang B. Pore characterization of organic-rich Lower Cambrian shales in Qiannan Depression of Guizhou Province, Southwestern China. *Mar Pet Geol*. 2015;62:28-43.
43. Brunauer S, Emmett PH, Teller E. Adsorption of gases in multimolecular layers. *J Am Chem Soc*. 1938;60(2):309-319.
44. Dubinin MM, Astakhov VA. Description of adsorption equilibria of vapors on zeolites over wide ranges of temperature and pressure. *Adv Chem*. 1971;102:69-85.
45. Barrett EP, Joyner LG, Halenda PP. The determination of pore volume and area distributions in porous substances. I. Computations from nitrogen isotherms. *J Am Chem Soc*. 1951;73(1):373-380.
46. Groen JC, Peffer L, Pérez-RamíRez J. Pore size determination in modified micro- and mesoporous materials. Pitfalls and limitations in gas adsorption data analysis. *Microporous Mesoporous Mater*. 2003;60(1-3):1-17.
47. Do DD, Do HD. Adsorption of supercritical fluids in non-porous and porous carbons: analysis of adsorbed phase volume and density. *Carbon*. 2003;41(9):1777-1791.

48. Curtis ME, Cardott BJ, Sondergeld CH, Rai CS. Development of organic porosity in the Woodford Shale with increasing thermal maturity. *Int J Coal Geol*. 2012;103:26-31.
49. Loucks RG, Reed RM, Ruppel SC, Hammes U. Spectrum of pore types and networks in mudrocks and a descriptive classification for matrix-related mudrock pores. *AAPG Bull*. 2012;96:1071-1098.
50. JrJ T, Damberger HH. *Internal surface area, moisture content, and porosity of Illinois coals: variations with coal rank*. Urbana, IL: Illinois State Geological Survey; 1976:1-44.
51. Fryer JR. The micropore structure of disordered carbons determined by high resolution electron microscopy. *Carbon*. 1981;19(6):431-439.
52. Hou J, Wang B, Zhang Y, Zhang J. Evolution characteristics of micropore and mesopore of different rank coal and cause of their formation. *Coal Geol Exploration*. 2017;45(5):75-81.

SUPPORTING INFORMATION

Additional supporting information may be found online in the Supporting Information section at the end of the article.

How to cite this article: Zhou S, Liu H, Chen H, et al. A comparative study of the nanopore structure characteristics of coals and Longmaxi shales in China. *Energy Sci Eng*. 2019;7:2768–2781. https://doi.org/10.1002/ese3.458